Spectroscopic investigation of the electronic structure of yttria-stabilized zirconia

Thomas Götsch,[1] Erminald Bertel,[1] Alexander Menzel,[1] Michael Stöger-Pollach,[2] and Simon Penner[1,*]

[1]*Institute of Physical Chemistry, University of Innsbruck, Innrain 52c, A-6020 Innsbruck, Austria*

[2]*University Service Centre for Transmission Electron Microscopy (USTEM), TU Wien, Wiedner Hauptstraße 8–10, A-1040 Vienna, Austria*

(Received 7 November 2017; revised manuscript received 18 January 2018; published 12 March 2018)

The electronic structure and optical properties of yttria-stabilized zirconia are investigated as a function of the yttria content using multiple experimental and theoretical methods, including electron energy-loss spectroscopy, Kramers-Kronig analysis to obtain the optical parameters, photoelectron spectroscopy, and density functional theory. It is shown that many properties, including the band gaps, the crystal field splitting, the so-called defect gap between acceptor (Y'_{Zr}) and donor ($V^{\bullet\bullet}_{O}$) states, as well as the index of refraction in the visible range exhibit the same "zig-zag-like" trend as the unit cell height does, showing the influence of an increased yttria content as well as of the tetragonal–cubic phase transition between 8 mol% and 20 mol% Y_2O_3. Also, with Čerenkov spectroscopy (CS), a new technique is presented, providing information complementary to electron energy-loss spectroscopy. In CS, the Čerenkov radiation emitted inside the TEM is used to measure the onset of optical absorption. The apparent absorption edges in the Čerenkov spectra correspond to the energetic difference between the disorder states close to the valence band and the oxygen-vacancy-related electronic states within the band gap. Theoretical computations corroborate this assignment: they find both, the acceptor states and the donor states, at the expected energies in the band structures for diverse yttria concentrations. In the end, a schematic electronic structure diagram of the area around the band gap is constructed, including the chemical potential of the electrons obtained from photoelectron spectroscopy. The latter reveal that tetragonal YSZ corresponds to a *p*-type semiconductor, whereas the cubic samples exhibit *n*-type semiconductor properties.

DOI: 10.1103/PhysRevMaterials.2.035801

I. INTRODUCTION

Doped zirconium oxides, such as yttria-stabilized zirconia (YSZ) are among the most widely used oxygen ion conductors. Their high ionic conductivity at elevated temperatures stems from the substitution of Zr^{4+} ions by Y^{3+} [1], which results in the formation of oxygen vacancies to maintain charge neutrality. This enables the transport of O^{2-} species [2,3]. Being efficient ion conductors, they are employed as electrolytes in chemical sensors or solid oxide fuel/electrolysis cells (SOFCs/SOECs). In the latter, YSZ is not only employed as electrolyte, but also often as anode constituent (traditionally together with Ni in the form of a cermet) [4]. There, the stabilized zirconium dioxide partakes in catalytic reactions—for instance, in steam reforming processes of hydrocarbon fuels.

In both cases, as electrolyte and as an electrode material, the electronic structure is the main property determining the performance. For example, it is desirable to lower the operating temperatures of SOFCs, which currently are in the range between 1073 and 1273 K, as it would enable the use of cheaper materials and also lower the operating costs [5]. This requires an improved ionic conductivity at lower temperatures. Also, at the electrode, a lower ohmic resistance would be beneficial as it would increase the current densities of the fuel cells. Both of these goals might be achieved using special co-doping of YSZ. However, in order to do that, the electronic structure of YSZ itself has to be mapped out in detail first, without relying on a purely theoretical approach.

The number of published studies regarding the electronic structure is low. For pure ZrO_2, there are some predominantly theoretical works, based on density functional calculations [6–9]. There are also some experimental investigations, which mainly focus on optical absorption using either UV/VIS spectroscopy [10–12], or ellipsometry [13]. Due to its increased complexity, fewer theoretical computations have been done on YSZ. Kul'kova and Muryzhnikova [14] calculated the densities of states for both YSZ and MgO-doped zirconia. Like for undoped ZrO_2, optical absorption measurements have been conducted, albeit fewer in number [15,16]. Also, French *et al.* have demonstrated that the determination of the optical (direct) band gap using UV/VIS absorption measurements does not lead to unambiguous results [10]. Wiemhöfer and Vohrer applied UV photoelectron spectroscopy and (ultra-high-vacuum) electron energy-loss spectroscopy [17], but they used different oxidic back contacts, which might influence the properties. Furthermore, apart from some thermodynamic properties concerning the back contact, they only measured the band gap and chemical potential for a single crystal and a thin film with very low concentration differences.

Here, we present a combination of systematic experimental and theoretical investigations of the electronic structure of YSZ as a function of the yttria content, allowing us to elucidate the effects of different dopant levels. For this, we employed sputtered thin film model systems, which previously have been shown to be representative specimens of YSZ [18–20]. Also, their unsupported nature excludes any possible influence of a

*simon.penner@uibk.ac.at

substrate on the analysis. In addition to that, the variation of the yttria content allows to get reliable information about the evolution of the electronic structure with the Y_2O_3 concentration. Because the same kinds of specimens are used with identical measurement techniques, large deviations as those found in the literature for different methods and sample types can be avoided. As samples, YSZ species with Y_2O_3 concentrations of 3 (3YSZ), 8 (8YSZ), 20 (20YSZ), and 40 mol% (40YSZ) are investigated. In a previous study [19], it was shown that the thin films of 3YSZ and 8YSZ were tetragonal, and that 20YSZ as well as 40YSZ led to cubic thin film specimens. Furthermore, the stoichiometry was shown to be the same in the thin films as in the target materials [19].

II. METHODS

A. Preparation of the thin films

For the deposition of the thin films, a home-built direct-current ion beam sputter source was employed [19]. The preparation was performed in a modular high-vacuum chamber (pumped by a turbomolecular pump as well as a baffle acting as a small cryopump) with a base pressure in the low 10^{-7} mbar regime. The sputter deposition was conducted in an argon background pressure of 5×10^{-5} mbar at a target voltage of -2000 V. As targets, powder pellets (10 mm diameter) were pressed onto tantalum spirals (required in order to mount the target in the source). To this end, a standard pellet press for infrared spectroscopy was operated at a compressive force of 20 kN. The powders employed were commercial YSZ samples (Sigma Aldrich) with Y_2O_3 contents of 3, 8, 20, and 40 mol%. The thin films, having nominal thicknesses of 25 nm, were deposited onto freshly-cleaved NaCl(001) single crystal substrates at 623 K to yield crystalline samples. The substrates were submerged in water afterwards to float off the thin films. These films were subsequently collected using TEM gold grids, resulting in unsupported YSZ thin films. For the photoelectron spectroscopy analyses, additional samples of comparable thicknesses were prepared on Si(111) wafers. Studies examining the composition as well as the crystal structures have already been performed in a previous work [19].

B. Characterization of the electronic structure

The electron energy-loss spectroscopy (EELS) and Čerenkov spectroscopy (CS) investigations were performed in a FEI Tecnai F20 S-TWIN (high-resolution) analytical (scanning) transmission electron microscope, operated at both 60 and 200 kV. This microscope was equipped with a Gatan GIF Tridiem energy filter and a Gatan Vulcan cathodoluminescence system.

All EELS measurements were conducted using a defocused beam with a probe size of approximately 50 nm, as the films were prone to charging. As a consequence, a better statistical sampling over multiple crystallites of this nanocrystalline material is gained. The low loss spectra were deconvoluted using the Richardson-Lucy algorithm [21], in order to remove the influence of the tail of the zero-loss peak (ZLP) from the onset of the interband transitions. The resulting full width at half maximum (FWHM) of the ZLP was used as a conservative estimation of the error bars.

The optical properties were obtained from the energy-loss spectra by first determining the energy-loss function, $\Im(-1/\varepsilon)$, from the single-scattering distribution, $S(E)$, with the help of the following formula [22]:

$$S(E) = \frac{I_0 t}{\pi a_0 m_0 v^2} \Im\left[-\frac{1}{\varepsilon}\right] \ln\left[1 + \left(\frac{\beta}{\theta_E}\right)^2\right], \qquad (1)$$

where I_0 is the zero-loss intensity, t is the specimen thickness, a_0 is the Bohr radius, m_0 is the electron rest mass, and v is the velocity of the electrons. In the last part, β describes the collection semiangle of the spectrometer and θ_E is the characteristic scattering angle for a given energy loss E. Subsequently, the real part was obtained via Kramers-Kronig analysis [21],

$$\Re\left[\frac{1}{\varepsilon}\right] = 1 - \frac{2}{\pi} P \int_0^\infty \Im\left[-\frac{1}{\varepsilon}\right] \frac{E' dE'}{E'^2 - E^2}, \qquad (2)$$

which then allowed the determination of the complex dielectric function,

$$\varepsilon = \varepsilon_1 + i\varepsilon_2 = \frac{\Re\left[\frac{1}{\varepsilon}\right] + i\Im\left[-\frac{1}{\varepsilon}\right]}{\left\{\Re\left[\frac{1}{\varepsilon}\right]\right\}^2 + \left\{\Im\left[-\frac{1}{\varepsilon}\right]\right\}^2}. \qquad (3)$$

The Gatan Vulcan spectrometer was utilized for Čerenkov spectroscopy. This consists of a specimen holder with two elliptic mirrors (each forming half an ellipsoid), with one being above the sample and one below. The specimen is in one of the focal points of this ellipsoid, while, in the second focal point, the optical fibers (one for each mirror) that lead to the spectrometer itself are located. Both mirrors can thus be read out separately, which allows the distinction between backscattered and forward-scattered radiation to be made.

For photoelectron spectroscopy [PES—using UV (UPS) as well as x-ray photons (XPS)], a Thermo Scientific MultiLab 2000 spectrometer was employed, reaching base pressures in the high 10^{-11} mbar to low 10^{-10} mbar range, fitted with a He plasma source (emitting the He I line at 21.2 eV), a monochromated Al K_α x-ray source (1486.6 eV) and an Alpha 110 hemispherical sector analyzer, equipped with seven channel electron multipliers. In order to determine the location of the chemical potential μ_e within the band gap of the semiconducting samples, the Fermi edge of a piece of palladium foil, brought into conductive contact with the thin film was recorded as well. This was done using the x-ray rather than the UV source due to its lower photon flux, resulting in less charging of the sample and thus smaller shifts of the spectra. Also, to correct for the contact resistance between the YSZ thin film and the Pd foil, the C 1s regions were recorded as well and the C-C components resulting from adventitious carbon were shifted to the same binding energy value. Thus the difference between the valence-band maximum of YSZ and the Fermi edge of Pd can be measured directly from the spectra. In all UPS experiments, a bias of -1.5 V was applied to the samples in order to accelerate slow electrons, improving the sharpness of the secondary electron cutoffs.

Using the following equation, the work function (Φ) can be derived from the UP spectra. ε describes the binding energies

relative to the valence-band maximum, while E and μ refer to the absolute energies of the respective levels:

$$\Phi = E_{\text{Vacuum}} - \mu_{\text{e}} = h\nu - (\varepsilon_{\mu_{\text{e}}} - \varepsilon_{\text{cutoff}}). \quad (4)$$

C. Density functional theory calculations

Density functional theory (DFT) calculations were carried out using scalar-relativistic projector-augmented waves (PAW) with the ABINIT code [23–27]. All calculations have been performed at the generalized gradient approximation (GGA) level using the PBE exchange and correlation functionals [28].

The cubic species (20YSZ and 40YSZ) were simulated utilizing $3 \times 3 \times 3$ supercells of the primitive fcc cell. In order to keep the calculation times at a manageable level, the tetragonal systems (3YSZ and 8YSZ) were described by a $2 \times 2 \times 2$ supercell of the conventional cells due to the larger number of atoms in the tetragonal cell, corresponding to a stoichiometry of 6 mol% Y_2O_3. The crystal structures were generated by stochastically replacing the required number of Zr atoms, n, by Y atoms as well as removing $n/2$ oxygen ions to form the vacancies (there is one oxygen vacancy per two yttrium ions to preserve a net charge of zero). The supercells are visualized in Ref. [29] and the lattice parameters and atomic positions are listed there as well (see Fig. S1 and Table S1).

Prior to the density of states (DOS) and band structure calculations, convergence studies regarding the wave function cutoffs for the coarse and fine grids, as well as the number of k points used for the integrations, were undertaken to ensure an accuracy of less than 0.1 meV. The cutoffs were subsequently set to 3800 and 5400 eV for the coarse and fine grids, respectively, and the number of k points was 54 for each polymorph. Geometry optimizations of the atomic positions and the unit cell volume, yielding residual forces of less than 5 meV nm^{-1} have also been conducted. The supercell band structures were unfolded to the respective primitive cells by means of the FOLD2BLOCH unfolding code [25]. The additional k points to be sampled for the unfolding process (taking into account the symmetries) were determined using the BANDUP tool [30,31].

III. RESULTS AND DISCUSSION

A. Conduction bands

Cubic YSZ, crystallizing in a fluorite structure [32], consists of edge-sharing [ZrO_8] cubes. According to crystal field theory, this results in a splitting of the Zr 4d (conduction) bands into two energetically lowered levels (e_g, formed by the $4d_{x^2-y^2}$ and $4d_{z^2}$ bands) and triply degenerate t_{2g} states (d_{xy}, d_{xz}, d_{yz}) that are raised in energy. The yttrium 4d levels are irrelevant in this consideration because they are located at higher energies, further away from the conduction-band minimum (CBM) and the Zr 4d levels. The tetragonal polymorph also exhibits a cubic Zr–O coordination, albeit a distorted one [33]. The distortion has negligible influence on the observed crystal field splitting.

Figure 1(a) displays the O K edge EEL spectra for the four specimens after background correction (exponential). In order to avoid introducing artifacts into the spectra, plural scattering was not removed. The band gaps are so large (see Sec. III B) that plural scattering in the region of interest (less than approximately 5 eV above the CBM) can be neglected. All the spectra show two prominent peaks in their fine structure, resulting from crystal field splitting. Even though the crystal-field-splitting stems from Zr d-states, it can be observed in the K-edge spectrum (where O 1s electrons are excited) because the bonding in ZrO_2 is highly covalent [8]. The resulting hybridization between the O 2p and Zr 4d bands admixes sufficient O 2p character into these states to yield a substantial transition matrix element.

The e_g and t_{2g} state maxima were located by fitting Gaussian peaks to the respective regions in the spectra. In Fig. 1(a), these fits are indicated by dashed lines. The energies of these states could then be measured relative to the conduction-band minimum (taken to be the inflection point of each ionization edge). These results are shown in Fig. 1(b). The lower panel depicts the e_g locations relative to the CBM. In the case of the tetragonal species, the e_g states move slightly towards the CBM with increased Y_2O_3 concentrations [0.86(10) and 0.80(10) eV for 3YSZ and 8YSZ, respectively], although the shift is well within the standard deviation. Upon the phase transition to the cubic system, this behavior changes: going from 20YSZ to 40YSZ, these states significantly move away from the CBM [from 0.85(10) eto 1.09(10) eV]. Comparing this plot to that of the t_{2g} states (upper panel), the major difference is that the spread of the values is much larger for the latter. Moreover, the trend displayed by the tetragonal and cubic films is now the same: the addition of yttria leads to an increase in the energies of the states. For the tetragonal solid solutions, this encompasses a change from 4.23(10) to 4.32(10) eV. During the crystal structure change from tetragonal to cubic between 8YSZ and 20YSZ, the yttria-related change of the t_{2g} energy is partly offset by the structural transformation. In the cubic phase, the t_{2g} energy increases from 4.42(10) to 4.97(10) eV.

The crystal field splitting as a function of the yttria content can be seen in Fig. 1(c). The splitting first increases from 3.37(10) eV (3 mol%) to 3.52(10) eV (8 mol%) before remaining constant when the phase transformation between 8YSZ and 20YSZ occurs. For the cubic films, it increases again with the yttria content, although the slope is smaller than for the tetragonal samples [from 3.57(10) to 3.88(10) eV].

In fact, the behavior displayed by the crystal field splitting is reminiscent of the unit cell height, as demonstrated in a previous study [19]. Based on the diffraction data from that work, an angular integration using the PASAD tool [34], with subsequent peak fitting of all reflexes was performed in order to get a statistically better sampling of lattice parameter values. Fig. 1(d) depicts that trend graphically. For 3YSZ, this lattice parameter c is 0.512(1) nm, whereas it increases to 0.522(2) nm when increasing the dopant level to 8 mol% Y_2O_3. 20YSZ, has a very similar unit cell height [0.520(1) nm], even though there is a significantly larger amount of yttria dissolved in the ZrO_2. This is due to the phase transformation into the cubic fluorite structure [19]. The unit cell height increases again towards 40YSZ, which features a lattice parameter of 0.525(3) nm. The striking similarities between unit cell height and crystal field splitting [Fig. 1(c)] demonstrate the intimate correlation between crystal field and geometry.

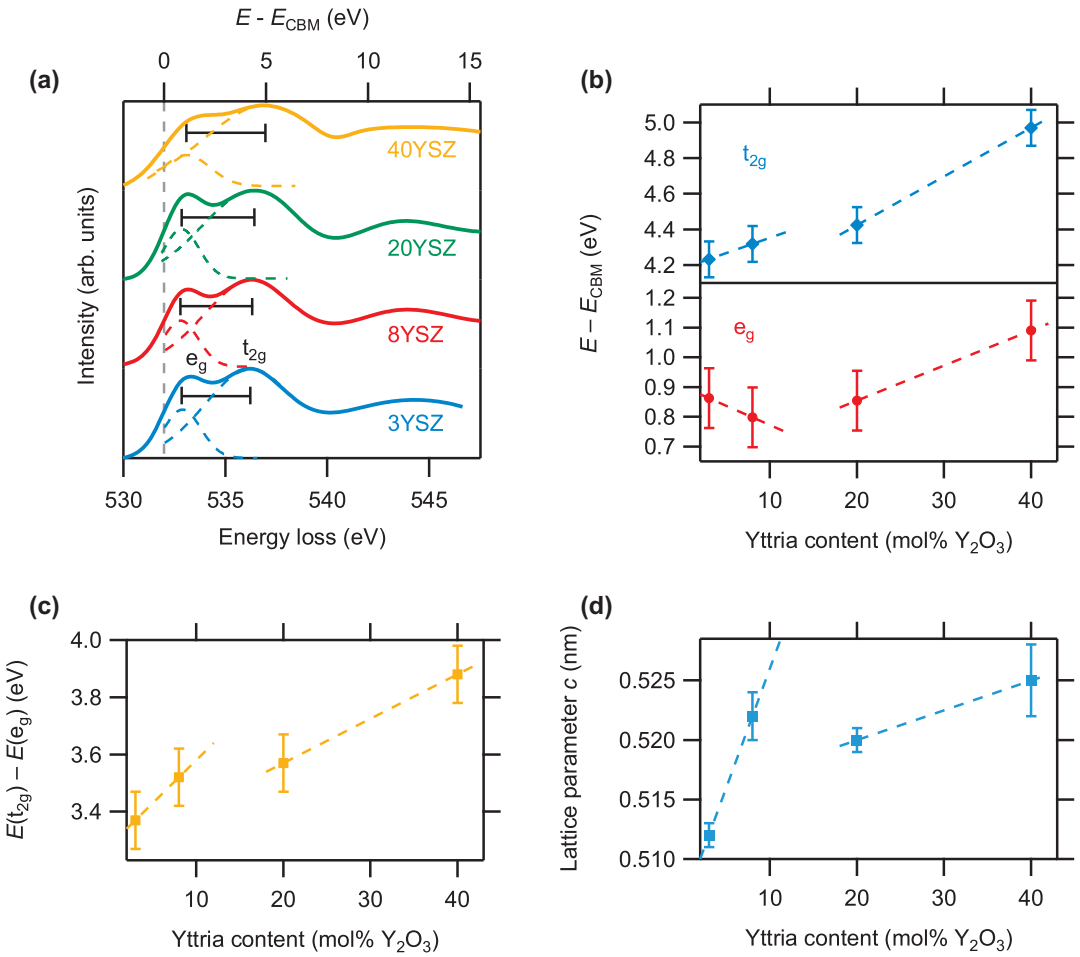

FIG. 1. (a) Oxygen K edge EEL spectra. (b) Positions of the e_g and t_{2g} levels relative to the conduction-band minimum. (c) The crystal field splitting. (d) The lattice parameter c (i.e., the unit cell height) as a function of the yttria content (based on data from Ref. [19]), exhibiting a similar trend to the crystal field splitting. The dashed lines in (b) through (d) serve as guides to the eye.

B. Band gaps

The low-loss regions of the EEL spectra mainly consist of the zero-loss peak at an energy loss of 0 eV (elastic scattering), interband transitions (i.e., excitation of valence electrons across the band gap) and, at slightly higher energies, plasmon features. The interband transitions allow the determination of the band gap by measuring the onset of these transitions. However, to avoid relativistic losses due to Čerenkov radiation masking the onset, the acceleration voltage had to be reduced to 60 kV during acquisition, so that the speed of the electrons was lower than the speed of light inside the medium (c/n) [35]. Furthermore, the influence of the tail of the zero-loss peak has to be removed from the region of interest by deconvolution via the Richardson-Lucy algorithm [21]. The resulting data are shown in Fig. 2(a). The slight increase in intensity visible between 1 and 2 eV is not due to an electronic transition, but is an artifact resulting from the deconvolution process. The real interband transitions start at losses of around 6 eV. A square root function, accounting for the density of states of the conduction band, was fitted to the onset. The fit is shown as dashed lines and the resulting onset energies are marked by the vertical solid lines.

Because, in the TEM, an objective aperture with a collection semi-angle of $\beta = 2.8$ mrad was inserted into the back focal plane of the specimen, the only transitions that are sampled are those with a momentum transfer corresponding to a scattering vector of $\Delta q < 2.8$ mrad. At a primary beam energy of 60 keV, this is equivalent to a maximum change in the wave vector of $|\vec{k}_{\text{limit}}| = 3.51\ \text{nm}^{-1}$. For comparison, the conventional unit cell of 20YSZ (cubic) has a lattice parameter of $a = 0.520$ nm [19]. Since the indirect band gap in cubic ZrO_2 stems from the X $\rightarrow$ Γ transition, i.e., from (1/2,1/2,0) to (0,0,0), it is associated with a wave vector difference of $|\vec{k}_{\text{X}\rightarrow\Gamma}| = 2\pi/a = 12.1\ \text{nm}^{-1}$ [36]. Hence the momentum transfer limit imposed by the objective aperture is significantly lower than the momentum required for the indirect transition ($|\vec{k}_{\text{limit}}|/|\vec{k}_{\text{X}\rightarrow\Gamma}| = 0.29$). It follows that the transition with the lowest energy in the spectrum is related to the direct band gap (X $\rightarrow$ X, see Fig. S2 in Ref. [29] for a visualization of the transitions probed in this experiment).

The band gaps are plotted in Fig. 2(b) for each Y_2O_3 concentration. The overall trend has—as expected—a reciprocal relation to the lattice parameter: the band gaps decrease with an increased amount of yttria, whereas there is a jump to larger

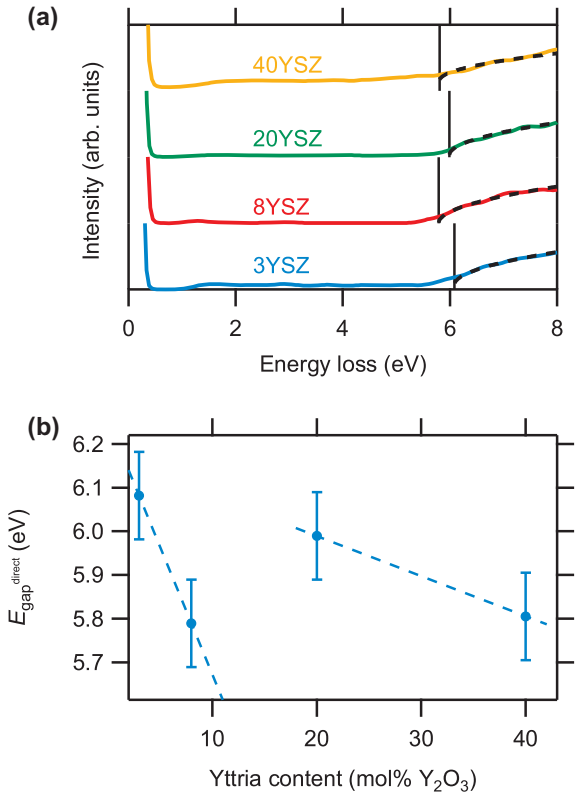

FIG. 2. (a) Low-loss valence EEL spectra. The onset of the interband transitions corresponds to the (direct) band gap. (b) The direct band gaps as a function of the Y_2O_3 concentration (with dashed lines to guide the eye). The trend of this plot is reciprocal to that exhibited by the lattice parameter [see Fig. 1(d)].

gaps at the point of the phase transition. The larger the unit cell, the smaller the band gap will be. By variation of the lattice parameter of a primitive cell of cubic ZrO_2, this relation is shown to actually be linear (see Fig. S3 in Ref. [29]).

For 3 mol% of Y_2O_3, the direct band gap is measured to be 6.08(10) eV. The value obtained by Nicoloso *et al.* [15] (5.7(1) eV) is slightly smaller. A possible reason is that their thin films used for the optical absorption studies were deposited on quartz substrates, while our specimens were unsupported in nature. Thus it is conceivable that their films were under stress. According to Fig. 2(b), 8YSZ has a direct band gap of 5.79(10) eV. This, on the other hand, is in excellent agreement with the value of 5.80(5) eV postulated by Nicoloso and coworkers [15], although they claim that their 8YSZ specimen is not tetragonal, but cubic—even though no diffraction data are shown. In light of the difficulties encountered when distinguishing the two polymorphs discussed elsewhere [19], this assignment has to be taken with a grain of salt. French *et al.* [10] obtained for their tetragonal sample (4.5 mol%) either 5.78 or 6.62 eV from the same data set, depending on which energy region they chose to use for their fit. Our interpolated value for this concentration would be 5.99 eV, just in-between those values. This demonstrates the difficulty of determining band gaps solely using UV/VIS spectroscopy.

The first of our cubic samples, 20YSZ, exhibits a direct band gap of 5.99(10) eV and for 40 mol% Y_2O_3, we obtain 5.81(10) eV. No literature values are available for these large yttria concentrations as most studies focus on specimens with approximately 8 mol%. However, we can extrapolate these band gaps, assuming a linear relationship, to lower Y_2O_3 contents. French *et al.* [10] obtained 6.1 eV for 9.5 mol% of yttria when analyzing UV/VIS spectra. At the same concentration, our extrapolation would yield 6.09(10) eV, which is in excellent agreement.

C. Optical properties

By removing plural scattering from the EEL spectra and subsequent calculation of the energy-loss function by Eq. (1), as well as Kramers-Kronig analysis [Eq. (2)], the complex dielectric function $\varepsilon = \varepsilon_1 + i\varepsilon_2$ can be obtained via Eq. (3). The real and imaginary parts thus derived are plotted in Fig. 3. At first glance, all ε look similar: at low energies, $\varepsilon_2 = 0$ due to the band gap, and ε_1, starting out at a slightly different value for each yttria concentration, increases rapidly until it reaches a maximum at the respective band gap energy, where ε_2 shows a sudden increase. Only the 40YSZ spectrum appears to be an exception to this, with the increase in ε_2 not being as immediate as for the other specimens, the peak being "smeared-out" and the onset of ε_2 starting as early as 2 eV. As was seen from EELS, however, this onset does not correspond to an electronic transition, but is an artifact resulting from the Richardson-Lucy algorithm. Although no better convergence of the Kramers-Kronig algorithm could be obtained for this sample, the spectra are included, since they contain all the features found in the other spectra. Absolute values of the specimen with 40 mol% Y_2O_3 cannot be compared to those of the others, though. Also, the minor peak found in the 20YSZ ε_1 spectrum at energies below 1 eV is not a physical feature, but stems from the deconvolution process as well. However, as it does not influence the optical properties in the visible range (the energy is too low for that), it can be ignored.

The most obvious differences occur in the energy region between 20 and 60 eV, which contains the volume plasmons and outer core levels (primarily Y and Zr $4p$). This region is highlighted in the insets. Focusing on ε_2 (dashed curves), the intensity ratio of the two peaks between 30 and 40 eV changes with increasing amounts of yttrium oxide: the higher the yttria content, the larger the first peak. The closest core levels to this energy region are, for both, Y and Zr, the $4p$ levels that, according to reference databases [37–39], are found at binding energies of 26 and 29 eV for Y and Zr, respectively, with respect to the metal Fermi level. In our samples, these transitions occur at higher energies because the excitonic states are strongly localized in oxides, leading to excitations into atomic multiplet states [40]. In fact, the respective transitions in our EEL spectra (approximately 33.5 eV and 39.0 eV for the Y and Zr $N_{2,3}$ edges) appear at the same energy losses as in literature spectra of ZrO_2 and Y_2O_3 [41].

Since the complex dielectric function, $\varepsilon = \varepsilon_1 + i\varepsilon_2$, can be described by [42]

$$\varepsilon_1 = n^2 - k^2 \text{ and} \tag{5a}$$

$$\varepsilon_2 = 2nk, \tag{5b}$$

multiple optical properties can be obtained from these data, including the index of refraction n, the extinction coefficient k, the absorption coefficient $\alpha = 2\omega k/c$ (with ω being the angular

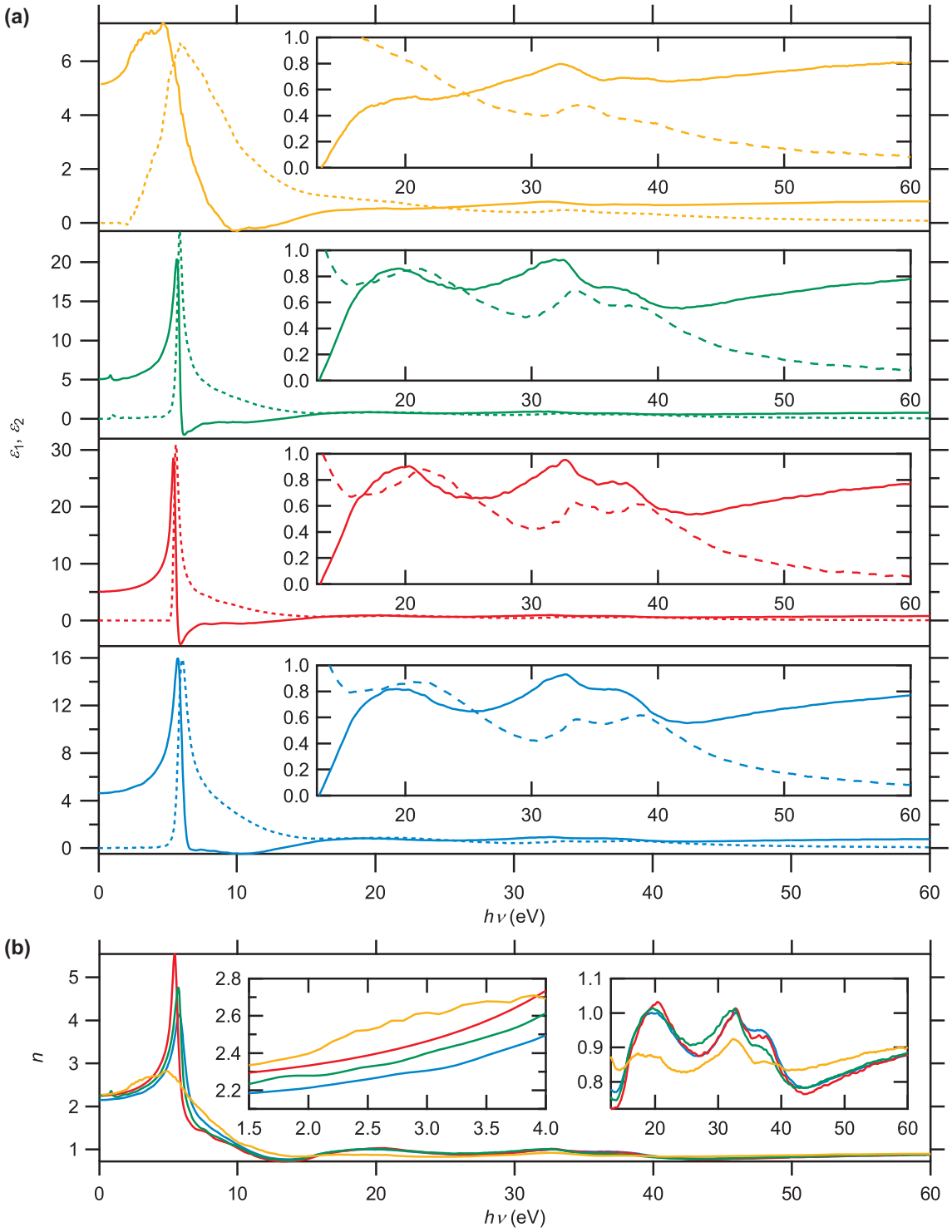

FIG. 3. Optical properties as a function of the Y_2O_3 content, obtained by Kramers-Kronig analysis. (a) Dielectric functions (with the real parts depicted by the solid lines and the imaginary ones rendered as dashed lines). (b) The index of refraction as derived from the data in (a). The insets in (a) and (b) highlight the respective functions in the region between 13 and 60 eV, as well as in the optical range for n.

frequency and c the vacuum speed of light), as well as the reflectivity R:

$$n = \left\{\frac{1}{2}\left[\left(\varepsilon_1^2+\varepsilon_2^2\right)^{1/2}+\varepsilon_1\right]\right\}^{1/2}, \tag{6a}$$

$$k = \left\{\frac{1}{2}\left[\left(\varepsilon_1^2+\varepsilon_2^2\right)^{1/2}-\varepsilon_1\right]\right\}^{1/2}, \tag{6b}$$

$$\alpha = \frac{2E}{\hbar c}\left\{\frac{1}{2}\left[\left(\varepsilon_1^2+\varepsilon_2^2\right)^{1/2}-\varepsilon_1\right]\right\}^{1/2} = \frac{2E}{\hbar c}k, \tag{6c}$$

$$R = \frac{(n-1)^2+k^2}{(n+1)^2+k^2}. \tag{6d}$$

For the index of refraction [Fig. 3(b)], the color-coding is the same as in Fig. 3(a), with 3YSZ being blue, 8YSZ red,

20YSZ green and 40YSZ orange. The two main regions of interest are displayed in the insets: the left one comprises the visible region and the near UV region, and the right panel focuses on the high energy region between 15 and 60 eV. In the visible region (left inset), the index of refraction exhibits a continuous increase for all samples, with only the 40 mol% deviating slightly due to the artifact resulting from the Kramers-Kronig analysis. The index of refraction for 3YSZ is lowest and it increases towards 8YSZ, drops again for 20YSZ before finally increasing again in 40YSZ, which is the same behavior as was found for the lattice parameter.

Wood *et al.* [43] reported on the indices of refraction in the visible and infrared regimes for various cubic YSZ single crystals prepared by skull melting. Their sample with 19 mol% of yttria has an index of refraction of 2.13 at 546 nm (corresponding to 2.27 eV), which is approximately 0.15 lower than our n (2.29 at 2.25 eV for 20YSZ). Our thin films are polycrystalline, Woods and coworkers used macroscopic single crystals. On the other hand, while our samples were shown to be impurity-free [19], there is no information regarding the purity of the single crystals used by Wood *et al.* (in particular, trace contamination from the crucibles could have an impact on the optical properties).

In Fig. S4(a) in Ref. [29], absorption-related properties are given. The extinction coefficient (upper panel) and the absorption coefficient (middle panel) exhibit similar features as ε_2. The reflectivities (lower panel), on the other hand, go through a maximum between the respective band gap values and approximately 10 eV, but then rapidly drop to very low values (below 0.05, i.e., 5% already at 20 eV). This is in line with the optical reflectivity measurements reported by French and coworkers [10].

The magnitude of the dielectric function within the visible range of the spectrum is displayed in the Supplementary Material in Fig. S4(b) as a function of the yttria content of the samples, where the color of the bars denotes the wavelength (compare the color bar to the right). Also, in the visible range, the index of refraction follows the same trend already exhibited by the lattice parameter. The Y-concentration dependence of n in the tetragonal specimens (3YSZ and 8YSZ) is significantly larger than in the cubic ones (20YSZ and 40YSZ).

Similarly, the index of refraction and the reflectivity also exhibit an analog trend as $k = 0$ [see Eq. (6d)], as can be discerned from Fig. S4(c), which is why we opted to not display them separately. Interestingly, the variation on n, Δn (from 780 to 380 nm), also shows the same trend.

D. Defect States

Defect states can, in principle, be detected via their absorption spectra under electron or photon irradiation. EELS, however, suffers from a substantial background, rendering the detection of low-intensity thresholds difficult. Here, we show that the absorption threshold of Čerenkov radiation, which is emitted inside a TEM when operated at high acceleration voltages, is a sensitive probe for electronic transitions within the band gap. This is due to the fact that Čerenkov radiation is not emitted for nonzero imaginary parts of the dielectric functions (ε_2, see below). The electronic structure of YSZ is expected to contain states within the band gap originating from both oxygen vacancies and the yttrium ions in the lattice, as, for instance, published by Wiemhöfer and Vohrer [17]. Since no such states could be observed using EELS, however, the Čerenkov radiation emitted inside the TEM was further analyzed using a Gatan Vulcan cathodoluminescence spectrometer. This instrument consists of a specimen holder with two mirrors: one above the sample and one below, which can be read out separately.

Čerenkov radiation, which was originally discovered by Pavel Čerenkov [44], can be described by placing a virtual cylinder around the electron and considering the energy passing its walls by means of the Bethe formalism [45]. For $r \to \infty$, the expression

$$\left(\frac{dE}{dx}\right) = \frac{e^2}{c^2}\Re\int_0^\infty \left(\mathrm{i}\sqrt{\frac{\lambda^*}{\lambda}}\right)\omega\left[1 - \frac{1}{\beta^2\varepsilon(\omega)}\right] \times \exp(-(\lambda+\lambda^*)r)\,d\omega \tag{7}$$

is obtained, with ω being the photon angular frequency and β describing the ratio of the velocity of the charged particle v and the vacuum speed of light c,

$$\beta = \frac{v}{c}. \tag{8}$$

λ is expressed via

$$\lambda = \frac{\omega}{v}\sqrt{1 - \beta^2\varepsilon(\omega)}, \tag{9}$$

and λ^* denotes its complex-conjugate. From Eq. (7), it can be shown that, while the expression becomes 0 for $r \to \infty$ (i.e., all the energy is absorbed by the material), this is not the case if λ was imaginary ($\Im\lambda = \lambda$): then, a finite amount of energy is not absorbed. Consequently, the following term within the brackets has to be purely imaginary [45],

$$\Re\left[\sqrt{\frac{\omega^2}{v^2}\left(1 - \beta^2\varepsilon(\omega)\right)}\right] = 0. \tag{10}$$

Equation (10) has two requirements in order to be fulfilled: first, the dielectric function ε must be real ($\varepsilon \in \mathbb{R}$), which, following Eq. (5), leads to

$$\varepsilon_2 = 0 \tag{11}$$

and, thus, $k = 0$. As a consequence, ε is related only to the index of refraction,

$$\varepsilon = \varepsilon_1 = n^2. \tag{12}$$

Furthermore, the condition postulated in Eq. (10) can only be true if the term inside the square root is negative, i.e., if $\beta^2\varepsilon(\omega) > 1$. Rewriting this by incorporating Eqs. (8) and (12) leads to

$$v > \frac{c}{n}, \tag{13}$$

that is, the velocity of the electrons has to be larger than the speed of light within the medium (i.e., the vacuum speed of light divided by the index of refraction).

According to Frank and Tamm [46], the number of photons for Čerenkov radiation per photon frequency and length traveled by the charged particle at velocity v can be described by

$$\frac{d^2N}{d\omega dx} = q^2\frac{\mu_{\mathrm{perm}}}{4\pi}\sin^2\theta. \tag{14}$$

Rewriting the conical angle, θ, as $\cos\theta = c/(vn)$, followed by integration with respect to ω, leads to

$$\frac{dN}{dx} = \frac{q^2}{4\pi}\int \mu_{\text{perm}}\left(1 - \frac{c^2}{v^2 n^2}\right) d\omega\,. \tag{15}$$

Because the number of photons emitted is required to be positive, the relation $v > c/n$ has to be fulfilled, which is the same condition that was derived from Eq. (10) (see also Sec. III B on EELS where this effect was to be avoided).

Čerenkov radiation is emitted in forward direction in a conical shape (with the angle θ, similar to a Mach cone); thus, the majority of it will only be detectable using the post-specimen mirror of the cathodoluminescence spectrometer. This is confirmed in Fig. S5 in Ref. [29], where the readouts of both mirrors are shown separately: while there is a strong signal in forward-direction, there is only baseline noise for the back-scattered photons, thus confirming the identity of the recorded radiation as Čerenkov radiation (in contrast to, e.g., cathodoluminescence, the emission of which would exhibit a spherical symmetry). Note, however, that it is possible for a small intensity of Čerenkov radiation to be detected in front of the specimen for thicker polycrystalline samples due to reflections on grain boundaries. The lack of cathodoluminescence in the spectra is due to the low thickness and the polycrystalline nature of our specimens: the predominant recombination processes are emission-less ones at surfaces and grain boundaries, rendering the remaining emission too low to be detected.

The Čerenkov intensities in Fig. 4(a) were acquired using a primary beam energy of 200 keV in order to fulfill Eq. (13). All spectra feature a drop to zero intensity between approximately 3.0 and 3.2 eV. This value is only half as large as the band gap, but it is in good agreement with the intra-band-gap structure that was also observed by Wiemhöfer and Vohrer [17]. The transition seen here correlates with the excitation from acceptor states close to the VBM, originating from the substitution of Zr^{4+} by Y^{3+}, into localized donor vacancy states ($V_O^{\bullet\bullet}$) that are close to the conduction-band minimum.

These defect-related excitation energies (ΔE^{defect}) are plotted as a function of the yttria content in Fig. 4(b). Similar to other properties, this graph strongly resembles that of the unit cell height: the more zirconium is replaced by yttrium, the larger is the energetic difference between the defect states. For 3YSZ, this results in an excitation energy of 3.109(3) eV, which increases to 3.150(3) eV at 8 mol% Y_2O_3. When the crystal structure changes from tetragonal to cubic, there is a significant drop to 3.049(8) eV for 20YSZ. Further increasing the dopant level to 40 mol% raises this energy again to 3.116(9) eV. Like for the crystal field splitting and the band gaps, the slope for the cubic specimens is also lower than for the tetragonal systems.

One reason that these transitions could not be seen in the EELS experiments is the large primary energy: the electron beam in the TEM has 60 keV, which is significantly larger than the defect-related excitation energies measured here (around 3 eV). This, combined with the low number of states available per unit cell, the thin sample and the spatial separation of the acceptor states and the oxygen vacancies, causes the transition matrix elements for this excitation to be too low for a peak to be discernible in the low loss EEL spectrum,

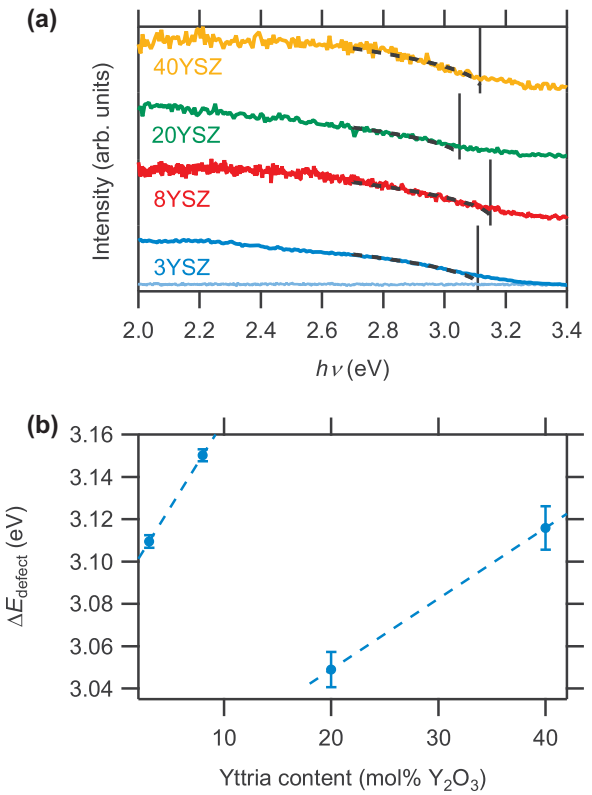

FIG. 4. (a) Čerenkov spectra, recorded using a cathodoluminescence spectrometer inside the TEM, reveal apparent absorption edges at energies well below those of the band gaps. The dashed curves represent the square root fits to the absorption edges and the solid vertical lines denote the onset of absorption. For 3YSZ, the baseline is shown as well (light blue). The choice of a highly dispersing diffraction grating for accurate threshold detection limits the spectral range shown in (a) to 1.4 eV. (b) The defect-related excitation energies as obtained from measuring the absorption edges in the Čerenkov data, with dashed lines as guides to the eye.

particularly in view of the required background deconvolution. Although the small transition matrix element gives rise to only small ε_2 values as well, the onset of the Čerenkov radiation occurs against zero background [see the spectrum of 3YSZ in Fig. 4(a), where the background is shown]. This results in a high sensitivity for excitations with low cross sections. Therefore, while this technique is limited to samples exhibiting a band gap, i.e., semiconductors and insulators, it serves as a powerful characterization tool, giving rise to information that is complementary to that obtained by EELS, with a vastly improved energy resolution (a few tens of meV) due to the detection of photons instead of electrons.

In order to check the assignment of the electronic transition found in CS, density functional theory calculations were performed. Figure 5 depicts the results of these computations. For comparison, Figs. 5(a) and 5(b) contain the band structures of the primitive unit cells of undoped tetragonal (a) and cubic (b) ZrO_2. The band structures are limited to the $\Gamma \rightarrow X$ transition because the direct band gaps measured by EELS are found in this region ($X \rightarrow X$ in the cubic case and $\Gamma \rightarrow \Gamma$ for tetragonal zirconia). The tetragonal unit cell contains more bands than cubic ZrO_2, which results from the larger amount

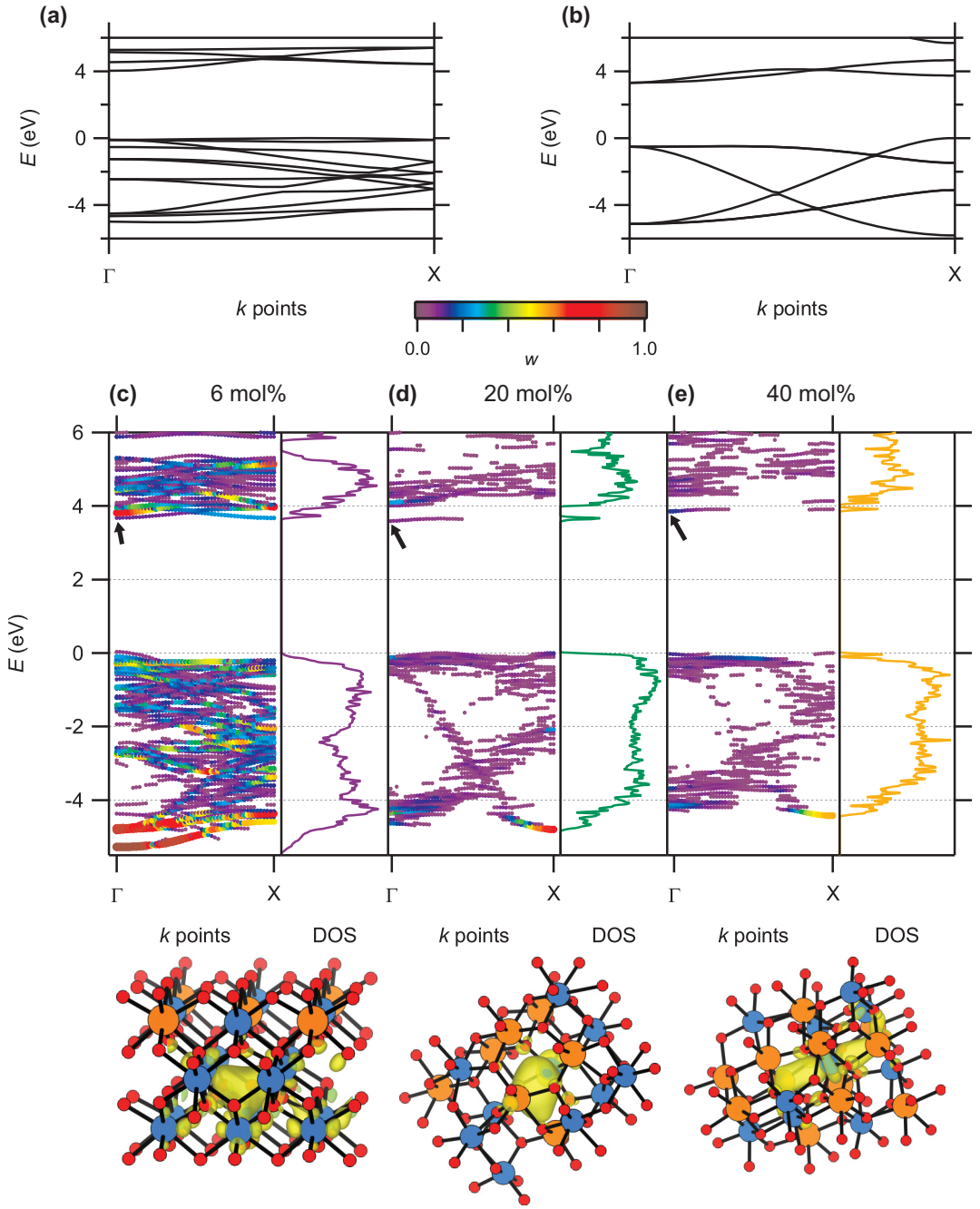

FIG. 5. Band structures of pure tetragonal (a) and cubic (b) ZrO_2, respectively. The unfolded band structures and densities of states of the doped systems, 6YSZ [(c), tetragonal], 20YSZ (d) and 40YSZ [(e), both cubic] are shown below. The color scale and point sizes depict the spectral weights w (only points with $w \geqslant 0.05$ are shown). The electron densities at the bottom represent the vacancy eigenstates at Γ that are marked in the band structure plots themselves (blue: Zr, orange: Y).

of formula units in the conventional cell as compared to the primitive cubic cell. Also, while the valence bands (comprising the oxygen $2p$ bands) of the cubic polymorph show distinct dispersions, as expected for p bands, the top-most bands in the tetragonal case (i.e., the ones closest to the VBM) appear very flat, in agreement with previously reported results [6,7]. Our results also reproduce the slightly lower energy of the $X \rightarrow X$ transition as compared to the $\Gamma \rightarrow \Gamma$ one for cubic zirconia. This is specific for relativistic calculations (Garcia *et al.* [6]), in contrast to nonrelativistic computations, which yield a lower transition at the Brillouin zone center (Γ).

The plots in Figs. 5(c) through 5(e) contain the band structures and densities of states (DOS) of the stabilized variants. Due to increased computational demands, the two tetragonal samples had to be replaced by another one containing 6 mol% Y_2O_3 since that could be calculated using a $2 \times 2 \times 2$ supercell as compared to the $3 \times 3 \times 3$ cells employed for the cubic species. The colors and sizes of the dots in the band structure plots represent the spectral weights,

$$w = \sum_n \left| \left\langle \Psi^{\mathrm{SC}}_{m,\vec{K}} \,\middle|\, \Psi^{\mathrm{PC}}_{n,\vec{k}} \right\rangle \right|^2 , \tag{16}$$

corresponding to the primitive character of the supercell state [25,30]. These are expected to be lower for levels introduced by the dopants in the supercells. To improve the clarity of the plots, eigenstates with $w < 0.05$ are omitted in the rendering of the band structures. Furthermore, the zero of the energy axis was set to the eigenvalue of the highest occupied state in each case. The panels below visualize the electron densities corresponding to the eigenstates marked in the respective band structure plots (all at Γ).

Figure 5(c) presents the band structure and DOS of tetragonal 6YSZ. The general features of the primitive cell [Fig. 5(a)], including the flat VBM, are reproduced well. An additional eigenstate is present above the VBM close to Γ. This state causes a shoulder at the VBM in the DOS and results from the Y substitution (the corresponding electron density is rendered in Fig. S6 in Ref. [29]). Also, the DOS of the conduction band features a distinct peak just below the CBM. At the same energy, a very flat state is present in the band structure plot (marked by the arrow). Its low dispersion is due to the strong localization of this state: the electron density, shown below the band structure, reveals that it is primarily localized at an oxygen vacancy.

For the cubic species in Figs. 5(d) (20 mol% Y_2O_3) and 5(e) (40 mol% Y_2O_3), the band structures look similar to the primitive cell band structure as well. The densities of states of 20YSZ and 40YSZ are very similar, with minor differences at the defect levels. In both cases, there are some acceptor states above the VBM, and for 40YSZ, they form a distinct spike in the DOS. Both structures contain multiple donor levels since multiple oxygen vacancies are present in the supercells (four for 20YSZ and eight for 40YSZ). The lowest states (marked by arrows) are found well below the CBM, resulting in peaks in the DOS that are separated from the conduction bands. The rest of the donor states are close to the CBM itself. All again feature very low dispersions, indicative of their localized nature, which the densities below the plots confirm.

The position of the vacancy states closer to the CBM contradicts results previously published by Kul'kova and Muryzhnikova [14], who found the corresponding eigenstate to be in the center of the band gap. However, we obtain the location postulated by them before any geometry optimization is performed; hence, we ascribe the discrepancy to their unrelaxed geometry. Furthermore, our results agree well with the schematic structure postulated by Wiemhöfer and Vohrer [17].

The differences between the calculated acceptor and donor states are larger than what was obtained from the Čerenkov spectra, especially considering that GGA notoriously underestimates band gaps. However, the trend exhibited by these computations follows that found using the Čerenkov radiation: from 6YSZ to 20YSZ, the energy difference between Y'_{Zr} and $V_O^{\bullet\bullet}$ is lowered from 3.61 to 3.52 eV, whereas it increases to 3.80 eV towards 40 mol%. Thus, even though the absolute values obtained from DFT are off, the trends are reproduced well.

E. Valence bands

Čerenkov spectroscopy was used to determine the energy separation between occupied acceptor and unoccupied donor states. In order to determine the energies of the acceptor states inside the band gap, UV photoelectron spectroscopy (UPS) was employed. In Fig. 6(a), the UP spectra are displayed. The zero of the energy axis was placed at the VBM. The spectra of the tetragonal samples on the one hand, and the two cubic specimens on the other are clearly distinct. In all cases, the lowest-energy peak at approximately 10 eV originates from the emission of secondary electrons (SE). The variation of the low-energy cutoff reflects the different work functions.

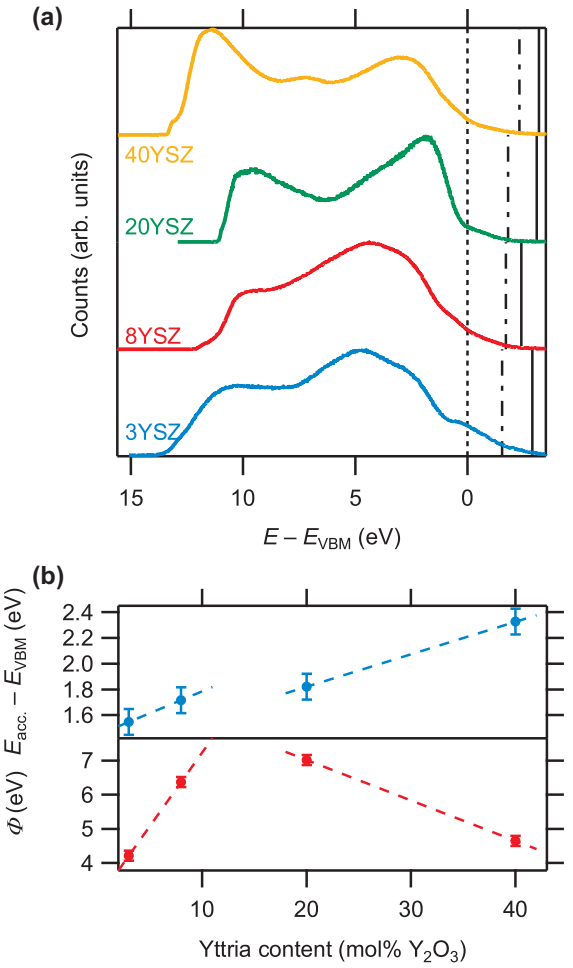

FIG. 6. (a) UV photoelectron spectra of YSZ for four different concentrations of Y_2O_3. The energy axis is scaled relative to the VBM (dotted line), while the dashed-dotted line denotes the maximum of the (occupied) acceptor states. The solid line represents the chemical potential (see Fig. 7). (b) The spread of the acceptor states $E_{acc.} - E_{VBM}$ (measured from the VBM, top panel) and the work function Φ (bottom panel), as determined from the UP spectra. The dashed lines in (b) serve as guides to the eye to visualize the trends.

The major peak in the 3YSZ spectrum (bottom spectrum) corresponds to the O $2p$ bands. The shoulder at approximately 0 eV is actually also present in the calculated DOS for 6YSZ [see Fig. 5(c)], albeit in a slightly less prominent form. The extrapolation of the low-binding-energy-side of the $2p$ peak to the baseline was used to determine the VBM. There is a finite DOS above the VBM. As already discussed earlier, this residual DOS in the band gap results from the yttria dopants

in the system. The maximum energy of these defect (acceptor) states, as obtained by linear extrapolation, is denoted by the dash-dotted line in Fig. 6(a). Accordingly, the width of the acceptor states for 3 mol% of Y_2O_3, is approximately 1.5(1) eV. The solid line on the far right of the spectrum represents the chemical potential, its determination will be explained below.

The valence band of 8YSZ (second from bottom) looks very similar to that of 3YSZ. The major difference is that the onset of the SE peak is shifted to lower binding energies, which indicates a larger work function. The main peak appears to consist of the same components as in the 3YSZ case, but the features observed for 3 mol% yttria are less well defined. Also, the spread of the acceptor states is increased compared to 3YSZ, now being 1.7(1) eV as measured from the VBM.

In the spectrum of the first cubic species, 20YSZ, the maximum intensity appears directly below the VBM, in agreement with the calculated DOS [see Fig. 5(d)]. The work function is still larger than for 8YSZ. The spread of the Y-related states has increased to 1.8(1) eV. For 40 mol% yttria, the work function drops again. The acceptor-state-related tail of the DOS reaches 2.3 eV into the gap and the intensity distribution below the VBM shows a less abrupt onset than for 20YSZ, which parallels the DFT results. The additional peak at approximately 7 eV binding energy is apparently a structure in the SE distribution since the valence band has only a width of slightly more than 4 eV.

The acceptor state widths, $E_{\mathrm{acc.}} - E_{\mathrm{VBM}}$, are shown in the upper panel of Fig. 6(b). These widths increase continuously, although there is an apparent stagnation between 8 mol% and 20 mol% Y_2O_3 [with the energy levels being 1.7(1) and 1.8(1) eV, respectively], that is related to the phase transition.

The work function values are plotted in the lower panel of Fig. 6(b). At 3 mol%, Φ is 4.2(1) eV, and increases to 6.4(1) eV at 8 mol% of yttria. In the cubic samples, it decreases from 7.0(1) eV for 20YSZ to 4.6 eV at 40 mol% Y_2O_3.

F. Chemical potential

The chemical potential μ_e in an insulator or a semiconductor, often also labeled as the Fermi energy E_F, is difficult to measure directly by photoelectron spectroscopy. However, it is still possible to measure its distance to the VBM by placing a metal next to the semiconductor and exploiting the fact that the chemical potentials align when two materials are brought into ohmic contact. However, a charging of the insulating thin film caused by its poor conductivity could still give rise to a potential drop between sample and reference and thus result in a shift in the chemical potentials. Thus, a piece of Pd foil was placed on top of the YSZ thin films, as shown schematically in Fig. 7(a). Measuring the valence-band spectra using a monochromated Al-K_α X-ray source enables the shift between the thin film and Pd to be corrected for by aligning the C–C components of the C 1s regions (originating from small amounts of adventitious carbon, which cannot be avoided when transferring the specimens to the UHV chambers) to the same binding energy [47]. Using x-rays has another advantage as the lower photon flux of the x-ray source compared to a UV source inhibits the occurrence of surface photovoltages [48,49]. Thus, with the respective carbon peaks

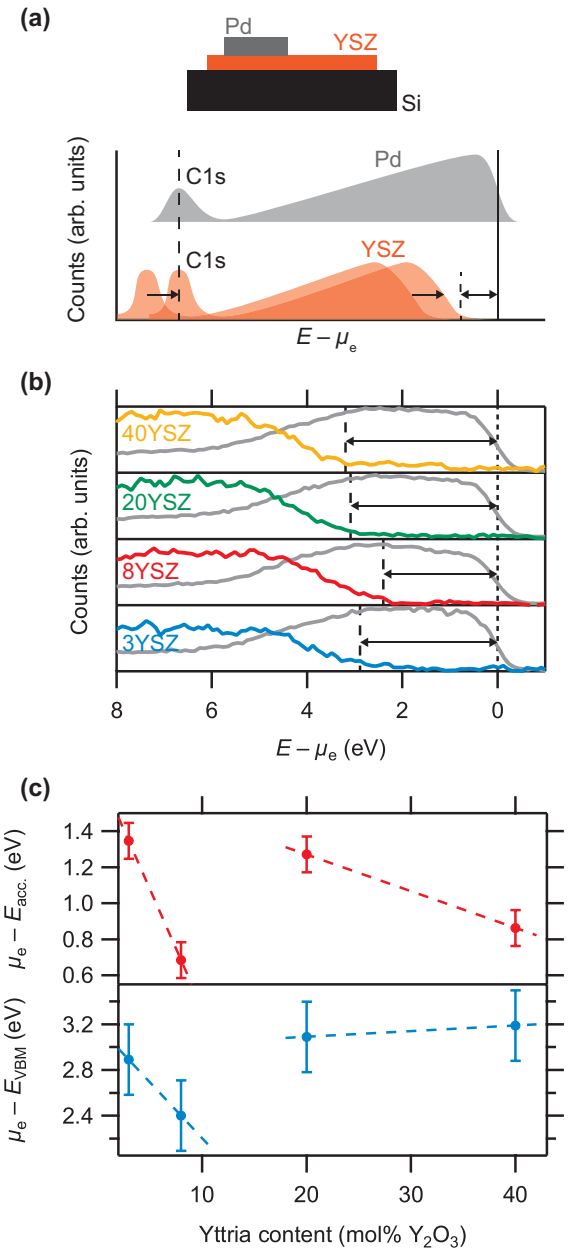

FIG. 7. (a) Scheme of how the location of the chemical potential μ_e within the band gap was determined for the YSZ samples by aligning the C 1s peaks (adventitious carbon) of the Pd and YSZ specimens, which enabled the determination of $\mu_e - E_{\mathrm{VBM}}$. (b) The YSZ valence band (color-coded) and Pd Fermi edge spectra (grey), already shifted appropriately. (c) Locations of the chemical potentials with respect to the VBM (lower panel) and the highest acceptor states (upper panel), with the dashed lines serving to display the trends.

aligned, the distance between the VBM and the Fermi level can directly be measured by overlaying the two respective valence-band spectra, as demonstrated in the lower panel of Fig. 7(a). The spectra for the YSZ specimens aligned in this way are displayed in Fig. 7(b). In each case, the location of the Pd Fermi edge was obtained by fitting a Fermi function to the Pd spectra. μ_e drops relative to the VBM with increasing Y concentration in the tetragonal samples, whereas it stays almost constant in the cubic samples.

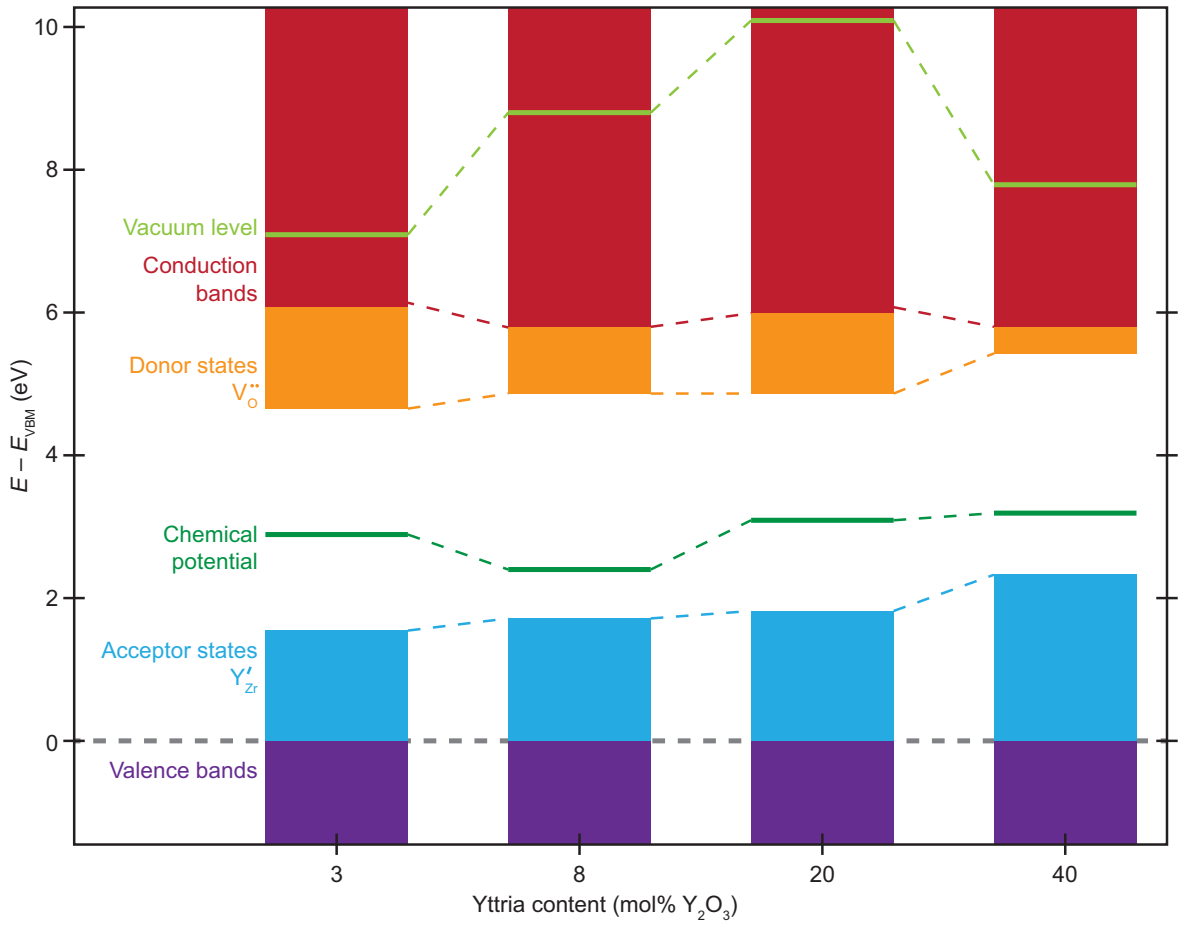

FIG. 8. Schematic summary of the electronic structure of 3YSZ, 8YSZ, 20YSZ, and 40YSZ close to the band gap, based on the experimental data shown previously. The dashed lines between the different concentrations are used as guides to the eye to better display the changes of the various parameters. The zero of the energy axis is placed at the VBM. The conduction bands are derived primarily from Zr 4*d* and 5*s* states. The latter are strongly dispersive (almost free-electron-like) and, therefore, extend to energies several eV above the CBM.

This behavior is summarized in the lower panel of Fig. 7(c). For the tetragonal samples, the chemical potential is just below the center of the band gap (48% and 42% for 3YSZ and 8YSZ, respectively), while it is just above the center in the case of the cubic specimens (52% and 55% for 20YSZ and 40YSZ). Despite YSZ containing both, *p* and *n* dopants, a weak *p*-type character prevails in tetragonal YSZ, whereas the *n* character is slightly stronger in cubic YSZ.

If, on the other hand, the chemical potential is not referenced to the VBM, but rather to the highest acceptor states (corresponding to the highest-lying occupied states in the system), the plot appears to be very different [top panel of Fig. 7(c)]. This reveals that μ_e shifts towards the acceptor state maximum with increasing Y_2O_3 content in both, the tetragonal and the cubic case. The structural change causes an additional offset away from the acceptor states. Thus the energy difference between these defect states and the chemical potential, $\mu_e - E_{acc.}$, exhibits the same type of behavior that was also observed for the band gaps and other properties.

G. Summary of the electronic structure

The vicinity of the band gap is displayed schematically in Fig. 8. There, the electronic states of the different

TABLE I. A summary of the electronic properties of each yttria concentration: the crystal field splitting [$E(t_{2g}) - E(e_g)$], the direct band gap as determined via EELS (E_{gap}^{direct}), the defect-related excitation energies from Čerenkov spectroscopy (ΔE_{defect}), the work function (Φ), chemical potential relative to the VBM ($\mu_e - E_{VBM}$), and the width of the acceptor states (Y'_{Zr}) $E_{acc.} - E_{VBM}$.

Yttria content mol% Y_2O_3	$E(t_{2g}) - E(e_g)$ (eV)	E_{gap}^{direct} (eV)	ΔE_{defect} (eV)	Φ (eV)	$\mu_e - E_{VBM}$ (eV)	$E_{acc.} - E_{VBM}$ (eV)
3	3.37(10)	6.08(10)	3.109(3)	4.2(1)	2.89(10)	1.5(1)
8	3.52(10)	5.79(10)	3.150(3)	6.4(1)	2.40(10)	1.7(1)
20	3.57(10)	5.99(10)	3.049(8)	7.0(1)	3.09(10)	1.8(1)
40	3.88(10)	5.81(10)	3.116(9)	4.6(1)	3.19(10)	2.3(1)

concentrations are aligned to the VBM, which highlights the evolution of the band gaps nicely. The vacancy/acceptor states are drawn as regions even though they are discrete niveaus, as indicated by DFT calculations, because we can only measure their lowest edges using Čerenkov spectroscopy. Also, since the specimens, especially those with larger yttria concentrations, contain multiple vacancies with different chemical environments (e.g. differing numbers of Zr/Y atoms as nearest neighbors, distance to the next vacancy etc.), it is conceivable that those eigenstates approach a continuum. This rendering also reveals that the lowest edge of the vacancy states moves closer to the CBM the more yttria is put into the system, whereas it is pulled down in energy by the change in the crystal structure. This is especially visible for 40YSZ, where the vacancy levels are very close to the conduction band. The reason could be that, with increasing Y_2O_3 concentration and, thus, also with increasing $V_O^{\bullet\bullet}$ concentration, more and more degenerate vacancy states are formed,rendering the chemical environments increasingly similar, and thus causing a lower spread in the energy of these states. Some of the electronic properties that were measured are summed up in Table I.

IV. CONCLUSION

A thorough characterization of the electronic structure of YSZ specimens with varying concentrations from 3 mol% to 40 mol% was presented, leading to the electronic structure diagram shown in Fig. 8. First, the crystal class was determined on the basis of the unit cell heights. This parameter exhibits a discontinuous behavior, making a distinction of the tetragonal and cubic samples possible [19]. The discontinuity is reflected in numerous electronic and optical properties.

EELS was employed to determine the direct band gaps. With values around 6 eV, our results agree well with literature. The increase of the yttria content decreases the band gap, which in turn correlates to the increase in the lattice parameter. Furthermore, the crystal field splitting determines the shape of the oxygen K edge, indicating a large degree of covalency in the sample, which enables O 1s $\rightarrow$ Zr 4d charge transfer excitations.

The optical properties of the system were determined by Kramers-Kronig analysis of the low-loss spectra. This investigation revealed that the index of refraction and the dielectric function exhibit the same behavior in the visible range that was displayed by the unit cell heights.

The dopant-related states were investigated using a new spectroscopic technique presented in this work, called "Čerenkov spectroscopy." This method makes use of the Čerenkov radiation that is emitted when charged particles traverse the sample at speeds larger than the speed of light within the medium. This radiation is only emitted up to the energies where the imaginary part of the dielectric function ε_2 increases from zero. Transitions that are inaccessible by other techniques can be probed with this form of spectroscopy. In the present case, the transition from the yttrium-induced acceptor states to the vacancy-related donor states was examined. As the Čerenkov effect only occurs in dielectric samples, this method cannot be used for metals, but it serves as a powerful tool for semiconductor/insulator research in order to sample the levels introduced by extrinsic doping.

The data provided here supply valuable information for future applications of this most widely used solid oxide electrolyte material. The knowledge of the electronic states, especially the vacancy states inside the band gap, allows for specific modifications of YSZ, e.g., by co-doping, in order to tune the properties to the desired values. For instance, the energy difference between the highest occupied (disorder) states and the Fermi level is lowest in 8YSZ (see Fig. 8). If additional acceptor states were to be introduced by another dopant species, the Fermi level could be lowered further, maybe even below some of the acceptor states. This in turn would boost the electronic conductivity. This is an important goal, for instance, in the application as solid oxide fuel cell anode.

ACKNOWLEDGMENTS

This work was financially supported by the Austrian Science Fund (FWF) via grant F4503-N16 and has been performed within the framework of the Forschungsplattform Materials and Nanoscience. The computational results presented were achieved using the Vienna Scientific Cluster (VSC).

[1] T. H. Etsell and Spyridon N. Flengas, Electrical properties of solid oxide electrolytes, Chem. Rev. **70**, 339 (1970).

[2] B. C. H. Steele and A. Heinzel, Materials for fuel-cell technologies, Nature (London) **414**, 345 (2001).

[3] N. Miura, T. Sato, S. A. Anggraini, H. Ikeda, and S. Zhuiykov, A review of mixed-potential type zirconia-based gas sensors, Ionics **20**, 901 (2014).

[4] A. Atkinson, S. Barnett, R. J. Gorte, J. T. S. Irvine, A. J. McEvoy, M. Mogensen, S. C. Singhal, and J. Vohs, Advanced anodes for high-temperature fuel cells, Nat. Mater. **3**, 17 (2004).

[5] D. Marinha, L. Dessemond, and E. Djurado, Comprehensive review of current developments in IT-SOFCs, Curr. Inorg. Chem. **3**, 2 (2013).

[6] J. C. Garcia, L. M. R. Scolfaro, A. T. Lino, V. N. Freire, G. A. Farias, C. C. Silva, H. W. Leite Alves, S. C. P. Rodrigues, and E. F. da Silva, Structural, electronic, and optical properties of ZrO_2 from ab initio calculations, J. Appl. Phys. **100**, 104103 (2006).

[7] H. Jiang, R. I. Gomez-Abal, P. Rinke, and M. Scheffler, Electronic band structure of zirconia and hafnia polymorphs from the GW perspective, Phys. Rev. B **81**, 085119 (2010).

[8] L. Soriano, M. Abbate, J. Faber, C. Morant, and J. M. Sanz, The electronic structure of ZrO_2: Band structure calculations compared to electron and x-ray spectra, Solid State Commun. **93**, 659 (1995).

[9] B. Králik, E. K. Chang, and S. G. Louie, Structural properties and quasiparticle band structure of zirconia, Phys. Rev. B **57**, 7027 (1998).

[10] R. H. French, S. J. Glass, F. S. Ohuchi, Y.-N. Xu, and W. Y. Ching, Experimental and theoretical determination of the electronic

structure and optical properties of three phases of ZrO_2, Phys. Rev. B **49**, 5133 (1994).
[11] C.-K. Kwok, Indirect band gap in α-ZrO_2, J. Vac. Sci. Technol. A **8**, 3345 (1990).
[12] E. Fernández López, V. Sánchez Escribano, M. Panizza, M. M. Carnasciali, and G. Busca, Vibrational and electronic spectroscopic properties of zirconia powders, J. Mater. Chem. **11**, 1891 (2001).
[13] J.-P. Xu, R.-J. Zhang, Y. Zhang, Z.-Y. Wang, L. Chen, Q.-H. Huang, H.-L. Lu, S.-Y. Wang, Y.-X. Zheng, and L.-Y. Chen, The thickness-dependent band gap and defect features of ultrathin ZrO_2 films studied by spectroscopic ellipsometry, Phys. Chem. Chem. Phys. **18**, 3316 (2016).
[14] S. E. Kul'kova and O. N. Muryzhnikova, Electronic structure and optical properties of zirconia, Inorg. Mater. **36**, 38 (2000).
[15] N. Nicoloso, A. Löbert, and B. Leibold, Optical absorption studies of tetragonal and cubic thin-film yttria-stabilized zirconia, Sens. Actuators B **8**, 253 (1992).
[16] G. Garcia, A. Figueras, R. I. Merino, V. M. Orera, and J. Llibre, Structural and optical properties of yttria-stabilized-zirconia films grown by MOCVD, Thin Solid Films **370**, 173 (2000).
[17] H.-D. Wiemhöfer and U. Vohrer, Spectroscopy and thermodynamics of electrons in yttria-stabilized zirconia, Ber. Bunsenges. Phys. Chem. **96**, 1646 (1992).
[18] T. Götsch, L. Mayr, M. Stöger-Pollach, B. Klötzer, and S. Penner, Preparation and characterization of epitaxially grown unsupported yttria-stabilized zirconia (YSZ) thin films, Appl. Surf. Sci. **331**, 427 (2015).
[19] T. Götsch, W. Wallisch, M. Stöger-Pollach, B. Klötzer, and S. Penner, From zirconia to yttria: Sampling the YSZ phase diagram using sputter-deposited thin films, AIP Adv. **6**, 25119 (2016).
[20] T. Götsch, T. Schachinger, M. Stöger-Pollach, R. Kaindl, and S. Penner, Carbon tolerance of Ni–Cu and Ni–Cu/YSZ sub-μm sized SOFC thin film model systems, Appl. Surf. Sci. **402**, 1 (2017).
[21] R. F. Egerton, *Electron Energy-Loss Spectroscopy in the Electron Microscope*, 3rd ed., The language of Science (Springer, New York, 2011).
[22] M. Stöger-Pollach, Optical properties and bandgaps from low loss EELS: Pitfalls and solutions, Micron **39**, 1092 (2008).
[23] X. Gonze, A brief introduction to the ABINIT software package, Z. Kristallogr. - Cryst. Mater. **220**, 558 (2005).
[24] X. Gonze, B. Amadon, P.-M. Anglade, J.-M. Beuken, F. Bottin, P. Boulanger, F. Bruneval, D. Caliste, R. Caracas, M. Côté, T. Deutsch, L. Genovese, Ph. Ghosez, M. Giantomassi, S. Goedecker, D. R. Hamann, P. Hermet, F. Jollet, G. Jomard, S. Leroux, M. Mancini, S. Mazevet, M. J. T. Oliveira, G. Onida, Y. Pouillon, T. Rangel, G.-M. Rignanese, D. Sangalli, R. Shaltaf, M. Torrent, M. J. Verstraete, G. Zerah, and J. W. Zwanziger, ABINIT: First-principles approach to material and nanosystem properties, Comput. Phys. Commun. **180**, 2582 (2009).
[25] X. Gonze, F. Jollet, F. Abreu Araujo, D. Adams, B. Amadon, T. Applencourt, C. Audouze, J.-M. Beuken, J. Bieder, A. Bokhanchuk, E. Bousquet, F. Bruneval, D. Caliste, M. Côté, F. Dahm, F. Da Pieve, M. Delaveau, M. Di Gennaro, B. Dorado, C. Espejo, G. Geneste, L. Genovese, A. Gerossier, M. Giantomassi, Y. Gillet, D. R. Hamann, L. He, G. Jomard, J. Laflamme Janssen, S. Le Roux, A. Levitt, A. Lherbier, F. Liu, I. Lukačević, A. Martin, C. Martins, M. J. T. Oliveira, S. Poncé, Y. Pouillon, T. Rangel, G.-M. Rignanese, A. H. Romero, B. Rousseau, O. Rubel, A. A. Shukri, M. Stankovski, M. Torrent, M. J. van Setten, B. van Troeye, M. J. Verstraete, D. Waroquiers, J. Wiktor, B. Xu, A. Zhou, and J. W. Zwanziger, Recent developments in the ABINIT software package, Comput. Phys. Commun. **205**, 106 (2016).
[26] M. Torrent, F. Jollet, F. Bottin, G. Zérah, and X. Gonze, Implementation of the projector augmented-wave method in the ABINIT code: Application to the study of iron under pressure, Comput. Mater. Sci. **42**, 337 (2008).
[27] F. Jollet, M. Torrent, and N. Holzwarth, Generation of Projector Augmented-Wave atomic data: A 71 element validated table in the XML format, Comput. Phys. Commun. **185**, 1246 (2014).
[28] J. P. Perdew, K. Burke, and M. Ernzerhof, Generalized Gradient Approximation Made Simple, Phys. Rev. Lett. **77**, 3865 (1996).
[29] See Supplemental Material at http://link.aps.org/supplemental/10.1103/PhysRevMaterials.2.035801 for additional information regarding the DFT calculations, the band gap measurements, more optical properties and visualized states from the band structures.
[30] P. V. C. Medeiros, S. Stafström, and J. Björk, Effects of extrinsic and intrinsic perturbations on the electronic structure of graphene: Retaining an effective primitive cell band structure by band unfolding, Phys. Rev. B **89**, 041407(R) (2014).
[31] P. V. C. Medeiros, S. S. Tsirkin, S. Stafström, and J. Björk, Unfolding spinor wave functions and expectation values of general operators: Introducing the unfolding-density operator, Phys. Rev. B **91**, 041116(R) (2015).
[32] D.-N. Wang, Y.-Q. Guo, K.-M. Liang, and K. Tao, Crystal structure of zirconia by Rietveld refinement, Sci. China, Ser. A: Math. **42**, 80 (1999).
[33] B. Bondars, G. Heidemane, J. Grabis, K. Laschke, H. Boysen, J. Schneider, and F. Frey, Powder diffraction investigations of plasma sprayed zirconia, J. Mater. Sci. **30**, 1621 (1995).
[34] C. Gammer, C. Mangler, C. Rentenberger, and H. P. Karnthaler, Quantitative local profile analysis of nanomaterials by electron diffraction, Scr. Mater. **63**, 312 (2010).
[35] M. Stöger-Pollach, H. Franco, P. Schattschneider, S. Lazar, B. Schaffer, W. Grogger, and H. W. Zandbergen, Cerenkov losses: a limit for bandgap determination and Kramers-Kronig analysis, Micron **37**, 396 (2006).
[36] G. Grosso and G. Pastori Parravicini, *Solid State Physics*, 2nd ed. (Elsevier, Waltham, Massachusetts, 2014).
[37] J. F. Moulder and J. Chastain, *Handbook of X-Ray Photoelectron Spectroscopy: A Reference Book of Standard Spectra for Identification and Interpretation of XPS Data* (Perkin-Elmer Corporation Physical Electronics Division, Eden Prairie, 1992).
[38] Casa Software Ltd, CasaXPS (2011).
[39] Gatan Inc., *A Chart of Inner Shell Loss Edge Types and Energies for Electron Energy Loss Spectroscopy* (1986).
[40] E. Bertel, R. Stockbauer, and T. E. Madey, Electron emission and ion desorption spectroscopy of clean and oxidized Ti(0001), Surf. Sci. **141**, 355 (1984).
[41] Gatan Inc., EELS *Atlas*, http://www.eels.info/atlas (2017).
[42] F. Wooten, *Optical Properties of Solids* (Elsevier Science, Burlington, 1972).
[43] D. L. Wood, K. Nassau, and T. Y. Kometani, Refractive index of Y_2O_3 stabilized cubic zirconia: Variation with composition and wavelength, Appl. Opt. **29**, 2485 (1990).

[44] P. Čerenkov, Visible glow of pure liquids under the influence of γ-rays, Dokl. Akad. Nauk SSSR **2**, 451 (1934).

[45] J. D. Jackson, *Classical Electrodynamics*, 3rd ed. (Wiley India, New Delhi, 2011).

[46] I. Tamm and I. Frank, Coherent radiation of fast electrons in a medium, Dokl. Akad. Nauk SSSR **14**, 107 (1937).

[47] A. E. Hughes and B. A. Sexton, XPS study of an intergranular phase in yttria-zirconia, J. Mater. Sci. **24**, 1057 (1989).

[48] M. Alonso, R. Cimino, and K. Horn, Surface Photovoltage Effects in Photoemission from Metal-GaP(110) Interfaces: Importance for Band Bending Evaluation, Phys. Rev. Lett. **64**, 1947 (1990).

[49] G. T. Williams, S. P. Cooil, O. R. Roberts, S. Evans, D. P. Langstaff, and D. A. Evans, High temperature photoelectron emission and surface photovoltage in semiconducting diamond, Appl. Phys. Lett. **105**, 061602 (2014).